INTERFACE

royalsocietypublishing.org/journal/rsif

Research

Cite this article: Gueriau P *et al*. 2020 Visualizing mineralization processes and fossil anatomy using synchronous synchrotron X-ray fluorescence and X-ray diffraction mapping. *J. R. Soc. Interface* **17**: 20200216.
http://dx.doi.org/10.1098/rsif.2020.0216

Received: 31 March 2020
Accepted: 3 August 2020

Subject Category:
Life Sciences–Physics interface

Subject Areas:
biogeochemistry, environmental science, evolution

Keywords:
(bio)mineralization, mineral/life interactions, exceptional fossilization, synchrotron imaging

Authors for correspondence:
Pierre Gueriau
e-mail: pierre.gueriau@hotmail.fr
Cristian Mocuta
e-mail: cristian.mocuta@synchrotron-soleil.fr

THE ROYAL SOCIETY PUBLISHING

Visualizing mineralization processes and fossil anatomy using synchronous synchrotron X-ray fluorescence and X-ray diffraction mapping

Pierre Gueriau[1,2,3], Solenn Réguer[1], Nicolas Leclercq[1], Camila Cupello[4], Paulo M. Brito[4], Clément Jauvion[5,6], Séverin Morel[6], Sylvain Charbonnier[6], Dominique Thiaudière[1] and Cristian Mocuta[1]

[1]Synchrotron SOLEIL, L'orme des Merisiers, Saint-Aubin BP 48, 91192 Gif-sur-Yvette Cedex, France
[2]Université Paris-Saclay, CNRS, ministère de la Culture, UVSQ, MNHN, Institut photonique d'analyse non-destructive européen des matériaux anciens, 91192 Saint-Aubin, France
[3]Institute of Earth Sciences, University of Lausanne, Géopolis, 1015 Lausanne, Switzerland
[4]Departamento de Zoologia, Instituto de Biologia/IBRAG, Universidade do Estado do Rio de Janeiro, R. São Francisco Xavier, 524-Maracanã, Rio de Janeiro 20550-900, Brazil
[5]Muséum national d'Histoire naturelle, Sorbonne Université, CNRS UMR 7590, IRD, Institut de Minéralogie, de Physique des Matériaux et de Cosmochimie, IMPMC, 75005 Paris, France
[6]Centre de Recherche en Paléontologie—Paris (CR2P UMR 7207), CNRS, Sorbonne Université, Muséum National d'Histoire Naturelle, 57 rue Cuvier, CP38, 75005 Paris, France

PG, 0000-0002-7529-3456; CC, 0000-0001-6030-8670; PMB, 0000-0002-4853-8630; CJ, 0000-0002-3245-8222; CM, 0000-0001-5540-449X

Fossils, including those that occasionally preserve decay-prone soft tissues, are mostly made of minerals. Accessing their chemical composition provides unique insight into their past biology and/or the mechanisms by which they preserve, leading to a series of developments in chemical and elemental imaging. However, the mineral composition of fossils, particularly where soft tissues are preserved, is often only inferred indirectly from elemental data, while X-ray diffraction that specifically provides phase identification received little attention. Here, we show the use of synchrotron radiation to generate not only X-ray fluorescence elemental maps of a fossil, but also mineralogical maps in transmission geometry using a two-dimensional area detector placed behind the fossil. This innovative approach was applied to millimetre-thick cross-sections prepared through three-dimensionally preserved fossils, as well as to compressed fossils. It identifies and maps mineral phases and their distribution at the microscale over centimetre-sized areas, benefitting from the elemental information collected synchronously, and further informs on texture (preferential orientation), crystallite size and local strain. Probing such crystallographic information is instrumental in defining mineralization sequences, reconstructing the fossilization environment and constraining preservation biases. Similarly, this approach could potentially provide new knowledge on other (bio)mineralization processes in environmental sciences. We also illustrate that mineralogical contrasts between fossil tissues and/or the encasing sedimentary matrix can be used to visualize hidden anatomies in fossils.

1. Introduction

Fossils mostly consist of the mineralized remains or impressions of organisms. Biomineralized tissues such as invertebrate shells or vertebrate bones and teeth, which are highly resistant to decay, form the bulk of the fossil record (note that they usually undergo physico-chemical changes during fossilization). Occasionally, decay-prone soft parts (e.g. muscles, nervous systems) or even entire soft-bodied organisms such as worms, jellyfish or squid are 'exceptionally' preserved, offering us a more detailed view into the past than skeletal remains

alone. Nonetheless, soft tissues rarely survive as organic components. Instead, their preservation results from poorly constrained mineralization processes such as the permeation of tissues by mineralizing fluids (permineralization) or the rapid *in situ* growth of minerals (authigenic mineralization) driven by the activity of bacterial decay [1]. Better constraining these taphonomic processes is critical for circumventing any potential fossilization bias (e.g. size, taxonomic or tissue sorting that affects exceptional preservation deposits [1,2]), and properly interpret these invaluable snapshots of past life.

The mineralogical characterization of such exceptionally preserved fossils was historically assessed through petrographic observations of thin sections, later complemented—or even replaced—by the use and/or development of the most cutting-edge techniques available. As a result, the mineralogical composition of a fossil is nowadays largely inferred indirectly from its elemental composition, usually obtained from scanning electron microscope (SEM) energy-dispersive X-ray spectroscopy and mapping (e.g. [3]) or laser ablation inductively coupled plasma mass spectrometry (e.g. [4]). More recently, improvement in synchrotron rapid scanning X-ray fluorescence (XRF), which produces two-dimensional distributions of major to trace elements for decimetre-scale objects, offers additional palaeobiological, palaeoenvironmental and taphonomic information [5–11].

By contrast, X-ray diffraction (XRD), which specifically identifies the minerals present is rarely used by palaeontologists as it requires destructive sampling and powder preparation, and often only provides limited spatial information in highly heterogeneous materials such as fossils. In a few studies, electron backscatter diffraction (EBSD), a SEM-based technique that provides information about the structure, crystal orientation (texture), phase or strain in materials (e.g. [12]), was used to disentangle mineralization processes in fossils. For instance, it revealed key insight into biological control of mineral formation in mollusks, brachiopods and trilobites [13] but also microfossils [14]. Nevertheless, EBSD is restricted to sample sizes accommodated by the SEM chamber, operates mostly in reflection such that it requires the preparation of a finely polished sample surface, and the electron beam only diffracts in the first few lattice layers (typically approx. 50 nm). Extracting information not restricted to the very surface (i.e. from the volume or bulk) can be achieved in transmission geometry, using a detector placed behind the sample. This requires high-energy X-ray beams adapted to the thickness of the material under investigation, and has been particularly used for the visualization of paintings hidden underneath layers containing heavy elements that prevent the use of XRF mapping (e.g. [15]). As for palaeontology, Mürer *et al*. [16] non-destructively reconstructed three-dimensional maps of mineral composition and hydroxyapatite orientation in small (1–2 cm) bones of early tetrapod and lobe-finned fish by combining XRD and computed tomography using very high-energy X-rays (86.6 keV) within a 12–72 h time frame acquisition. Lower X-ray energies of 6–30 keV (commonly available at XRD synchrotron beamlines) enable imaging in two dimensions of the mineralogical structure and microtexture of thinner samples or sections, e.g. of modern and archaeological otoliths, within a reasonable time frame (typically approx. 10 min for 32 kilopixel images; approx. 5 h for megapixel images) and coupled to XRF mapping [17].

Here, we assess the potential of XRD mapping for investigating mineralization processes in the fossil record, using four fossils representing a wide range of (i) taxonomic affinities (arthropods, sarcopterygians and actinopterygians), (ii) types of preservation (compressed and three-dimensional fossils, including extensive soft-tissue mineralization) and (iii) ages and depositional environments. We produce megapixel mineralogical maps across millimetre-thick cross-sections through three-dimensional-preserved fossils and pluri-centimetre compressed fossils (up to 5×3 cm^2 lateral area). Insights into mineral identification and distribution at the microscale over large areas, as well as crystallite orientation and size in fossils show great promise for taphonomic and anatomical studies.

2. Material and methods

Mineralogical maps were collected synchronously with X-ray fluorescence maps at the DiffAbs beamline of the SOLEIL synchrotron source (France), owing to the development of a fast and multi-technique data acquisition platform at the SOLEIL synchrotron (the FLYSCAN platform [18]).

2.1. Experimental setup

Synchronous synchrotron rapid scanning X-ray fluorescence and diffraction mapping (SRS-XRFD) was performed using an incident X-ray beam of 16.2 or 18 keV, monochromatized using a Si(111) double-crystal monochromator, with a beam size diameter reduced down to 50 or 100 µm using platinum pinholes, or focused down to approximately 10 µm using Kirkpatrick–Baez mirrors [19]. XRF was collected using a four-element silicon drift detector (SDD, Vortex ME4, Hitachi High-Technologies Science America, Inc., total active area: 170 mm^2) oriented at 90° to the incident beam, in the horizontal plane. XRD was collected in transmission geometry using a two-dimensional hybrid pixel detector (XPAD S140, 240×560 pixels of 130 µm each [20–23]), which is placed behind the sample at a distance of typically 200–300 mm such to intercept diffraction rings over an angular range of approximately 7° in scattering angle (2θ). Several images can be collected along the 2θ angle by moving the detector in order to extend the available 2θ domain; one can also settle for a single detector position using *a priori* knowledge of the fossil composition to select a 2θ domain encompassing the diffraction peaks of interest (note that larger detectors can be used to cover a wider domain; e.g. [15,16]). Details about detector design, geometry, calibration, correction of the images and diagram (or profile) reconstructions from the corrected images are available in [23,24] and references therein. Figure 1*a* shows a schematic view of the setup.

Two-dimensional scanning was done by moving laterally the fossils in a plane rotated around the vertical axis by 20° to the primary beam (i.e. incident angle), to limit X-ray beam footprint on the sample but also such that the sample exhibits its surface to the SDD (no shadowing of the reflected XRD signal, figure 1*a*). Mapping over the entire fossils at a 35–100 µm lateral resolution was performed on the fly using the FLYSCAN platform [18]. A full XRF spectrum and one or several XRD images were collected at each pixel.

2.2. Data processing

2.2.1. Image generation and phase identification

XRD images were processed through self-written routines (azimuthal data regrouping along ψ direction) to extract their respective diffractograms (intensity versus 2θ profiles), and generate four-dimensional datasets (x, y, 2θ, intensity) and then particular XRD contrast maps. Phase identification and 2θ calibration were performed using powder XRD diffractograms obtained on fragments of the sedimentary matrix (and of the fossil when possible) using the

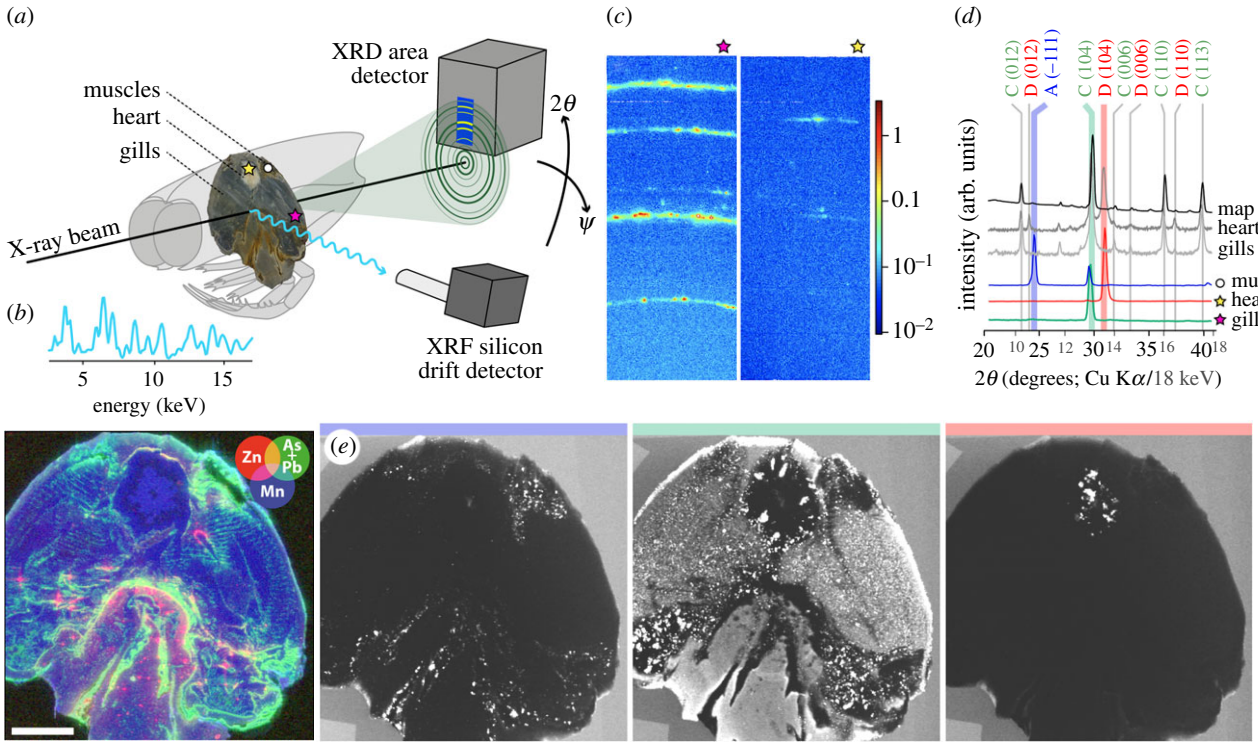

Figure 1. SRS-XRFD of a millimetre-thick transversal section of the thylacocephalan arthropod *Dollocaris ingens* (specimen MNHN.F.A66910) from the La-Voulte-sur-Rhône Lagerstätte (Jurassic, France). (*a*) Schematic view of the setup; while laterally scanning the sample with a high-energy X-ray beam, an XRD image (blue square) is collected at each pixel using a two-dimensional area detector that intercepts portions of the diffraction rings (red). Simultaneously, an XRF dataset is also acquired in reflection. (*b*) Mean XRF spectrum from a 25-pixel area around the beam location (top), and false colour overlay of zinc (red), arsenic and lead (green) and manganese (blue) distributions (bottom). (*c*) XRD images from pixels in the gills and heart, showing contrasting peaks. (*d*) Mean diffractograms extracted from the XRD map for three different 25-pixel areas in the gills, heart and muscles (colours; acquired at 18 keV), sum diffractogram from the map (black; acquired at 18 keV), and powder XRD diffractograms obtained from the gills and heart of a more anterior section of the same specimen (grey; acquired at Cu Kα). C, D and A phases are calcite, dolomite and arsenopyrite, respectively. (*e*) XRD intensity maps for 2θ (18 keV) = 10.68° (blue), 13.07° (green) and 13.68° (red), showing different mineralogical contrasts associated with the diffraction peaks highlighted by the corresponding colours in (*d*). Acquisition parameters: 9×11 µm^2 (H × V) beam spot size, 75×75 µm^2 scan step, 108 900 pixels, 150 (XRF) and 180 (XRD) ms couting times per pixel (total acquisition time 4 h 51 min). Scale bar = 5 mm.

Match! software (Crystal Impact) making use of the International Centre for Diffraction Data (ICDD) PDF 2015 database. Additional peaks in the XRD maps could then be identified using Match/ICDD database, as well as from the elemental information provided by the XRF data. All mineralogical and elemental distributions presented herein correspond to integrated intensities from the main XRD and XRF peaks, represented using linear (except figure 1*b*, logarithmic) grey or colour scales that go from dark to light, respectively, for low to high intensities. By Gaussian fitting the 2θ profile of XRD peaks attributed to different crystalline phases, corresponding crystallite sizes were extracted (for each pixel of the maps) by converting their full width at half maximum (FWHM) using Scherrer's formula. It was assumed that only the crystallite size is contributing to the broadening, and an instrument resolution function measured as approximately 0.035° (amounting several 10%, and up to 50% of the measured peak FWHM) was also taken into account for FWHM deconvolution.

2.2.2. Local texture measurements

In order to confirm some microstructure results obtained using the local probe XRD approach, supplementary local texture measurements were performed on a 'rod'-shaped sample (approx. $24 \times 1.5 \times 1.5$ mm^3 H × W × L) extracted using a diamond wire saw (figures 2*a* and 3*a*).

A texture measurement allows retrieving information about the orientation of the crystallites in the sample: for a fixed 2θ position of the detector (i.e. accessing a particular inter-reticular distance), the sample is oriented in all positions in the angular space. This is done by scanning it in azimuth (φ, rotation around the sample surface normal) and elevation (ψ, rotation around the projection of the impinging X-ray beam on the sample surface), while recording, at each position, the X-ray scattered signal. The resulting intensity is represented in a map, in polar coordinates (azimuth angle and elevation, e.g. figure 3*f–h*). In this way, when one or several crystallites are oriented such that the Bragg law is fulfilled for the particular inter-reticular distance probed (or the particular Bragg angle 2θ), high signal is found in the particular corresponding regions of the polar map, allowing: (i) to retrieve the particular orientation of the grains (φ, ψ) and (ii) to possibly quantify the volume ratio of that particular orientation, compared to other orientations on the map.

Rapid texture measurements were performed using the area detector (XPAD). The sample was illuminated by the impinging X-ray beam (of size approx. 150×150 µm^2 in this case) and the azimuth (φ) and elevation (ψ) angles were scanned, the first one continuously. An image was recorded in each $\varphi\psi$ point, then texture maps for various 2θ angles (i.e. volumes) were reconstructed [24]. Then, a similar dataset was recorded at the next vertical position on the sample. A rod-shaped sample is required in this case due to the azimuthal rotations during the measurements: as for the transmission XRD experiment, the sample dimension along the transmitted beam path needs to be relatively small (approx. 1.5×1.5 mm^2 in this case). This approach is expected to give volume texture information with a lateral resolution of about 150–200 µm along the sample long dimension.

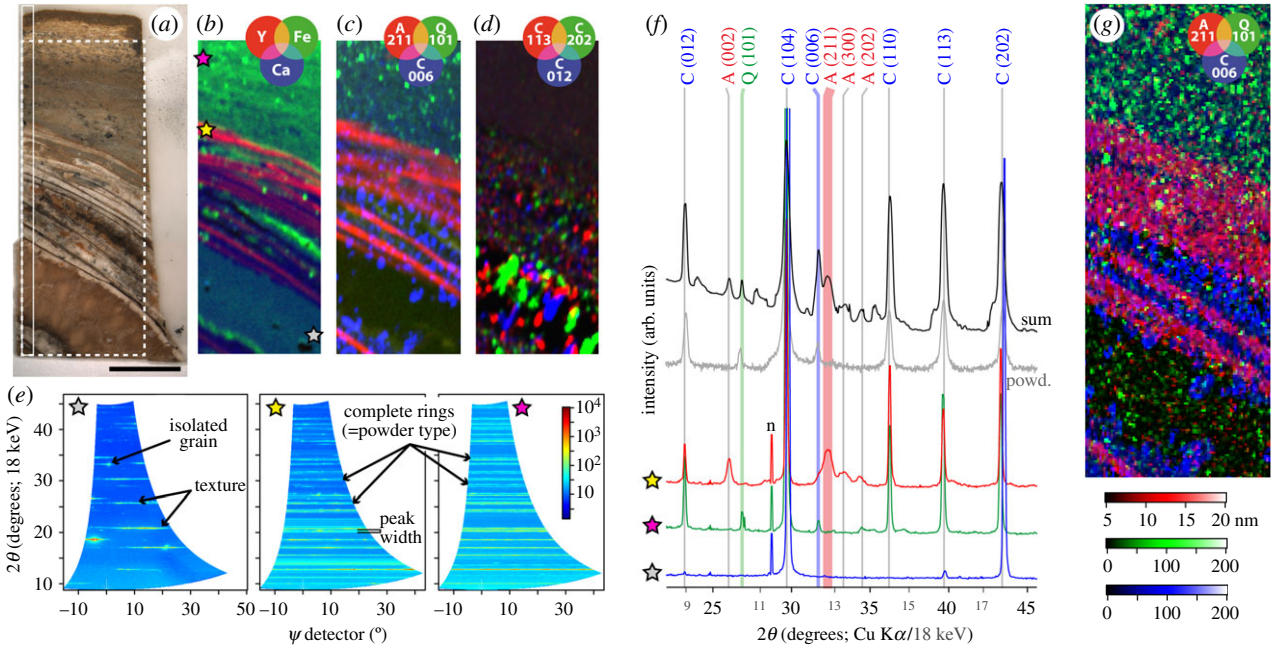

Figure 2. SRS-XRFD of a millimetre-thick transversal section through the lung plates of the coelacanth *Axelrodichthys araripensis* (specimen UERJ-PMB 143) from the Santana Formation of the Araripe Basin (Lower Cretaceous, northeastern Brazil). (*a*) Optical photograph of the section. Scale bar = 5 mm. The dotted and solid box areas, respectively, indicate the area imaged in (*b–d*,*g*) and the location where the rod-shaped sample in figure 3 was extracted. (*b*) False colour overlay of yttrium (red), iron (green) and calcium (blue) distributions from XRF. (*c*) False colour overlay of XRD intensity maps for 2θ (18 keV) of apatite (211) (red; 12.70°), quartz (101) (green; 10.40°) and calcite (006) (blue; 12.47°). (*d*) False colour overlay of calcite crystalline planes (113) (red), (202) (green) and (012) (blue) intensity maps showing large intensity fluctuations attributed to texture. (*e*) Combined XPAD images for the three areas identified by stars in (*b*) after conversion to (2θ–ψ) coordinates. (*f*) Mean diffractograms extracted from the XRD map for the three 24-pixel areas identified by stars in (*b*) (colours; acquired at 18 keV), sum diffractogram from the map (black; acquired at 18 keV), and a powder XRD diffractogram obtained from the sedimentary matrix (grey; acquired at Cu Kα). (*g*) Overlay of apatite (211) (red), quartz (101) (green) and calcite (006) (blue) crystallites size. Acquisition parameters: 100×100 µm^2 (H × V) beam spot size, 100×100 µm^2 scan step, 25 894 pixels (slightly cropped herein), 45 (XRF) and 37.3 (XRD) ms counting times per pixel (total acquisition time 34 min). The XRF and XRD data were acquired simultaneously.

2.3. Samples

The potential of this approach is illustrated using four fossils from different localities representing a wide range of taxa (an arthropod, a sarcopterygian and two actinopterygians), ages (Mesozoic and Cenozoic), sedimentary environments (concretions, shale, limestone), preservation types (compressed and three dimensions, including extensive soft-tissue mineralization) and mineralogical compositions (carbonates, phosphates, metal sulfides and oxides). Three-dimensional fossils of the arthropod *Dollocaris ingens* Van Straelen, 1923, and the superimposed lung plates of the coelacanth *Axelrodichthys araripensis* Maisey, 1986 were prepared as millimetre-thick cross-sections using a diamond disc saw. For *A. araripensis*, the fossil was embedded in resin, and we additionally extracted a 'rod-shaped sample' (mentioned above), so that five samples have actually been studied herein. Compressed specimens of the osteoglossomorph *Laeliichthys ancestralis* Santos, 1985, and of the cyprinodontiform *Prolebias goreti* Sauvage, 1878, were thin enough for X-ray transmission and were, therefore, mapped without any preparation. Age, locality, accession number, preservation, sedimentology and sample preparation information are available in table 1.

3. Results and discussion

3.1. Identification and distribution of minerals at the microscale

XRD mapping successfully produced contrasts, with peak positions and intensities varying depending on the sample composition (figure 1). Nonetheless, unlike in rotating powder XRD, only polycrystalline materials can here display all peaks (orientations); not all the crystalline planes are in position to diffract the incident beam in non-polycrystalline phases. This can be seen by the rather 'speckle' feature of the XRD rings (figure 1*c*). Quantitative phase analyses (using Rietveld refinement), therefore, can usually not be performed here, yet SRS-XRFD allows fine phase identification (figure 1*d*; constrained by XRF collected synchronously, and additional powder XRD diffractograms collected on the sedimentary matrix surrounding the fossil, or fragments of the fossil itself when possible), and offers the capability to image their distribution with less than 100 µm lateral resolution over centimetric lateral sized samples (figure 1*e*).

Figure 1 shows 100-kilopixel mineralogical maps collected from a millimetre-thick transversal section of the thylacocephalan arthropod *D. ingens* (specimen MNHN.F.A66910), clearly displaying the heart, muscles and gills preserved (figure 1*a*, *b*). This fossil, as well as most others from the deep-water ecosystem of La Voulte [25,26], exhibits a unique preservation style where most labile soft tissues are three-dimensionally retained in a complex mineral association including sulfides [27], providing pivotal information about the affinities and lifestyle of several fossil groups including thylacocephalans [28]. Wilby *et al*. [27] proposed a taphonomic scenario, including a diagenetic sequence of mineral precipitation, where apatite served as 'a template for calcification and pyritization'. Nonetheless, many details of the anatomy of these fossils have been lost, indicating that there are unidentified fossilization biases.

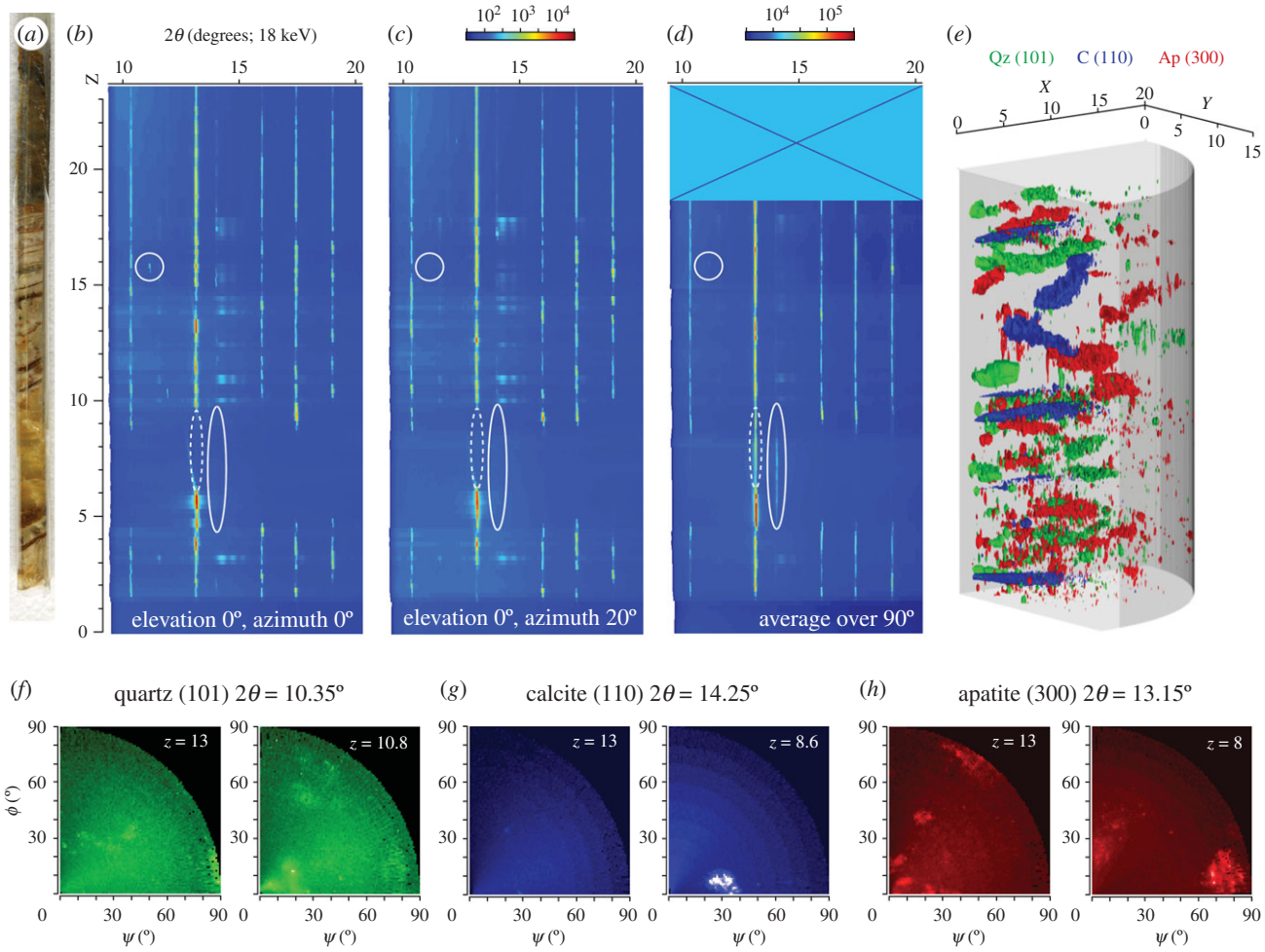

Figure 3. Pole figures along a rod-shaped sample extracted from the section through the lung plates of *A. araripensis* (specimen UERJ-PMB 143) shown in figure 2*a*. (*a*) Optical photograph of the sample. (*b*,*c*) Integrated 2θ intensities along the sample (*z*-axis), represented as colour map (logarithmic colour scale, from blue to red) for a fixed elevation (0°) and two particular azimuths, 0° (*b*) and 20° (*c*). Note the presence of the XRD 'gap' in the sample region $z = 5$ to 9 mm. (*d*) 2θ intensities averaged over 90° azimuth and elevation ranges. Regions where XRD peaks are different between panels (*b*) and (*c*), or only detected in (*d*), are highlighted by the circles and ellipses, respectively. (*e*) Three-dimensional representation as iso-surfaces of pole figures along the sample, for particular peaks corresponding to apatite (300, $2\theta = 13.15°$; red), quartz (101, $2\theta = 10.35°$; green) and calcite (110, $2\theta = 14.25°$; blue). (*f*–*h*) Pole figures ($\log_{10}$ scale, first quadrant only) for quartz (101) (*f*), calcite (110) (*g*) and apatite (300) (*h*) at z = 13 mm (left) and another *z* position where an XRD 'slab' can be seen in the three-dimensional view (colour code as in figure 2*g*, using identical amplitudes for each 2θ). All the measurements were performed at an X-ray beam energy of 18 keV.

In this context, Jauvion *et al*. [29] used SRS-XRFD in combination with optical and electronic microscopies, EDX, powder XRD and speciation X-ray absorption spectroscopy, to investigate fossilization biases in the abundant *D. ingens*. Indirect (SEM-EDX, XRF) and direct (XRD) mineralogical characterization allowed the authors to identify and locate the various phases comprising the fossils, showing that histologically similar tissues were replaced by the same minerals under fast biodegradation [29].

XRD precisely identified that cuticle and muscle fibres are preserved in fluorapatite, and epithelia-rich tissues (gills, digestive gland) in pyrite and pyrrhotite [29]. Arsenopyrite is also present in muscle, as well as in the appendages, where they underlie muscular structures (figure 1*e*, blue). Calcite is observed in the external part of the heart, but also where no organ is morphologically preserved and in the surrounding matrix (figure 1*e*, green). Dolomite is only found in the centre of the heart (figure 1*e*, red). Contrasting with the scenario proposed by Wilby *et al*. [27], data from MNHN.F.A66910 and several other specimens rather suggest that sulfide minerals and apatite precipitated concomitantly [29].

From a taphonomic point of view, localizing the different phases at the microscale over the entire organism (or here cross-section) is instrumental in defining a taphonomic sequence. Moreover, pinpointing tissue-specific mineralization processes is crucial for understanding taphonomic biases. The fact that different tissue types are replicated in a certain mineral emphasizes that fossilization processes are not homogeneous across the whole fossil, hence, a lack of favourable conditions for these minerals to precipitate might result in the loss of a whole group of tissues. Last but not least, identifying the precise mineralogical nature of phases has allowed Jauvion *et al*. [29] to better constrain precipitation-favourable physico-chemical parameters, and therefore reconstitute the fossilization environment.

3.2. Additional taphonomic information embedded in the X-ray diffraction images

Besides crystalline phase identification and their spatial distribution, the XRD data also contain information about the material structure and microstructure (figure 2). This is

Table 1. Age, preservation, sedimentology and nature of the studied samples. Institution abbreviations: MNHN.F, palaeontology collection of the Muséum national d'Histoire naturelle, Paris, France; UERJ, Universidade do Estado do Rio de Janeiro, Rio de Janeiro, Brazil.

species	taxonomy	age	locality	accession no.	preservation and sedimentology	sample nature	figure
Dollocaris ingens	Arthropoda, ?Crustacea, †Thylacocephala	Callovian (~165 Ma)	La-Voulte-sur-Rhône (France)	MNHN.F.A66910	carapace in three dimensions (incl. internal organs and part of appendages) within a metalliferous carbonate concretion	prepared millimetre-thick cross-section	1*a*
Axelrodichthys araripensis	Vertebrata, Sarcopterygii, Actinistia	Aptian/Albian (~110 Ma)	Araripe Basin (Brazil)	UERJ-PMB 143	lung ossified plates and void-infilling in three dimensions within a carbonate concretion	prepared millimetre-thick cross-section	2*a*
						prepared 'rod'-shaped sample	3*a*
Laeliichthys ancestralis	Vertebrata, Actinopterygii, Osteoglossomorpha	Barremian (~125 Ma)	Sanfransiscana Basin (Brazil)	099-PV-DZ-UERJ	compressed skeleton (incl. scales) in a soft, ferruginous paper shale	unprepared compressed fossil on thin slab	5*a*
Prolebias goreti	Vertebrata, Actinopterygii, Cyprinodontiformes	Rupelian (~30 Ma)	Apt-Céreste-Forcalquier Basin (France)	MNHN.F.CRT255	compressed skeleton hidden within a fine-grained limestone	unprepared compressed fossil on thin slab	5*d*

particularly interesting for mapping over pluri-centimetric areas, as shown herein, as the incident beam spot size used is much larger than the size of the crystallites constituting the fossil and its surrounding sedimentary matrix. In this case, XRD images acquired by the area detector can show (i) continuous rings (though sometimes slight speckle-like features are clearly visible), which result from diffraction of powder-like polycrystalline phases (i.e. random-oriented small crystallites), (ii) ring segments that evidence texture (preferential crystalline orientation) and (iii) spots (disposed on the corresponding ring) that indicate isolated grains (figure 2*e*). In turn, would the beam size be of similar size or smaller than the crystallites (i.e. when using micrometre or nanometre beams for very high-resolution analyses) only spots will potentially appear on the XRD images, if and only if the illuminated crystallite is in the right geometrical orientation to fulfil diffraction condition. In addition, the peak width is depending on the corresponding crystallite sizes (inversely proportional, i.e. the smaller the crystallites the wider the diffraction peaks [30]) and the local/micro-strain. In the absence of the latter the width of the diffraction peaks can, therefore, be converted to crystallite sizes (along a direction which can be retrieved from the geometry of the experiment), allowing to produce maps using crystallite size as a contrast signal (figure 2*g*).

Such results are illustrated against a millimetre-thick transversal section through superimposed lung plates of the coelacanth *A. araripensis* (specimen UERJ-PMB 143) from the approximately 110-million-year-old Santana Formation of the Araripe Basin, Brazil (figure 2*a*). A peculiarity of coelacanths is indeed the presence of a lung covered by ossified plates, described for almost all coelacanth taxa ranging from the Palaeozoic to the Recent [31–34]. Enriched in yttrium (figure 2*b*), suggesting an apatite composition [35], these plates are confirmed to be of apatitic bone nature by SRS-XRFD (figure 2*c*,*f*), as previously recognized from the observation of cellular bone with star-shaped osteocytes and a globular mineralization [33]. While hardly visible on the optical photograph, elemental and mineralogical maps further show that inner lung plates (i.e. the lowest plates in figure 2*a–c*, closer to the lung) are thinner than outer plates, confirming previous observations on ground thin cross-sections [31,36], and suggest that, most probably, these superimposed elements are formed first from the region closer to the lung surface than the outermost region. Note that the section has been prepared transversally through a crushed lung (see [31, text-fig. 2D]) and as such the cutting plane had little geometric impact on the plate thickness. The plates cover a calcium-rich area (figure 2*b*) made of large grains of calcite (figure 2*c*,*d*) exhibiting important texture (figure 2*d*,*e*) evidencing an infilling of the void created by lung decay. The surrounding carbonate concretion includes clay and quartz minerals (figure 2*b*,*c*).

Apatite peaks from the lung plates are much wider than calcite and quartz peaks (figure 2*f*), indicating that the plate crystallites are much smaller than those in the lung infill and the concretion. Crystallite size extraction shows that apatite crystallites from the lung plates yield a homogeneous size of approximately 10–15 nm, whereas calcite and quartz crystallites are an order of magnitude larger and less uniform in size (approx. 50–150 nm) (figure 2*g*). These data are totally in accordance with the homogeneity of the ossified, compacted and dense lung plates composed by true cellular bone tissue with osteocytes and globular mineralization, separated by layers of coarser limestone matrix,

observed in thin sections [31,33]. Lung plates of adult specimens of *A. araripensis* are constituted only by thin layers of homogeneous and compact bone tissue, contrasting to other coelacanth taxa (such as *Swenzia latimeriae* Clément, 2005) that may display, in addition, a non-mineralized region composed of a collagenic packet of microfibrils [33].

In view of the large inhomogeneities observed in crystallite size maps at different sample locations (figure 2*g*, see e.g. missing information in areas shown as dark background), the data highlight the existence of a significant, and variable, crystallite orientation, which is far from being that of a randomly oriented powder. Indeed, extended two-dimensional diffractograms at particular points in the sample (figure 2*e*) show, as mentioned before, the presence of XRD segments instead of isotropic rings. For highly textured samples, performing XRD measurements at fixed sample geometry could result in missed crystallinity information: crystallites corresponding to a particular phase are never in diffraction condition, thus no XRD corresponding peaks are detected. In order to illustrate this issue, a first XRD experiment was performed on the aforementioned rod-shaped sample (figure 3*a*): the sample was scanned along the vertical direction (z), at fixed azimuth and elevation angles (φ, ψ), and, in each point, XRD datasets were recorded (figure 3*b*,*c*). One can already note that, for the two shown measurements, the diffractograms for two azimuths exhibit presence/absence of some XRD peaks at particular z-coordinates (see e.g. the domain highlighted by circles in figure 3*b*,*c*). Thus, such a simple measurement does not ensure accessing all the characteristic XRD peaks and potentially might miss some of them. To overcome this issue, texture measurements were performed at each z position. A first way to exploit the texture datasets consists in extracting, for each z sample position, the XRD signal as the summation of all the corresponding XPAD images (azimuth and elevation angles). This approach ensures that all crystallites are brought into diffraction condition and potentially diffract, and it is now expected to obtain, from our illuminated volume (approx. $0.15 \times 1.5 \times 1.5$ mm^3), a diffractogram corresponding to that of a random powder (figure 3*d*). The most striking differences are the presence, in the aforementioned texture map, of XRD peaks in the z-range 5–9 mm (calcite void-infilling of the lung cavity) for 2θ values around 14° and 18° (unbroken ellipses in figure 3*b–d*); they were completely missing in all the tested fixed azimuth (0–80° range, every 20°) and fixed elevation (0°) configurations (line scans). Surprisingly, some apatite appears also associated with calcite in this region (dotted ellipses in figure 3*b–d*), likely to represent fragments of ossified plates that collapsed in the void left by the decay of the lung, or possibly phosphatized remains of the lung or soft tissues, common in the Santana Formation [37,38].

Full data exploitation of texture measurements is achieved through the generation of pole figure volumes (five-dimensional datasets, φ, ψ, 2θ, z, intensity). At particular 2θ scattering angles characteristic of the crystalline phases of interest (figure 2*f*), pole figures at each z-coordinate are extracted (e.g. figure 3*f–h*). The result is shown as a volume in figure 3*e*, in which pole figures along the z-direction and for particular 2θ angles (and thus different crystalline structures) are shown as three-dimensional iso-surfaces. This clearly demonstrates that missing information in areas such as the calcite void-infilling of the lung cavity that arose as dark background in figure 2*g* (z-range 5–9 mm in figure 3) results from an absence of diffraction in the used geometry (see how XRD peaks are not missed anymore in the pole figure volume; figure 3*e–h*). This three-dimensional visualization further reveals a layered structure of the sample, particularly visible for the calcite void-infilling of the lung cavity. Several other regions in the sample deserve a closer look. Around $z \sim 13$ mm, crystallite orientation is much more pronounced, as seen by the presence of localized scattered signal (hot spots) in the particular polar maps (figure 3*f–h*). In the case of the calcite void-infilling, the signal is much more diffuse and its position slowly rotates in φ and ψ, as illustrated in the three-dimensional view (blue surface figure 3*e*). The crystallites of all the phases identified can rotate with large amplitudes of several 10°, having variable preferential orientation, for different z positions on the sample. This is illustrated by the two pole figures extracted for the apatite (taken 5 mm apart): the scattered intensity is grouped (within 10–20°) around ($\varphi \sim 45°/\psi \sim 10$, 40 and 90°) and ($\varphi \sim 0°/\psi \sim 75°$ and $\varphi \sim 90°/\psi \sim 20°$), respectively (figure 3*h*).

Although this clearly shows the potential limitations of XRD mapping performed at fixed sample angles, one has to keep in mind not only the much longer time needed to perform such data acquisitions, but also the particular (rod-shaped) sample preparation required. *Sensu stricto*, the hypothesis of perfectly random-oriented polycrystalline phases does not hold. Yet, in the case of samples such as the fossils investigated herein, crystallite orientation still spans over several 10°, ensuring that the various crystalline phases (and related information such as the average crystallite size, see above) can be detected (though possibly only partially) even for fixed sample angular positions.

Considering now the above remarks, we can assume that texture is also visible in the mineralized heart of the three-dimensional-preserved thylacocephalan MNHN.F.A66910 (figures 1*e* and 4): speckly regions of the calcite and dolomite maps are probably characteristic of large size grains, possibly with specific orientations. Elongated crystals of calcite with alternating, ordered orientation grew at the periphery of the heart, while the centre has been replaced with much poorly organized dolomite (figures 1*e* and 4). This reveals a two-steps sequence of mineralization within the heart, contrary to the supposed coprecipitation with calcite in Jauvion *et al*. [29], which was tested possible with geochemical modelling. Moreover, the same model suggests calcite dissolution and dolomite precipitation while a later oxidation event is taking place, which might have been the case locally.

From a taphonomic point of view, the latter example shows how crystallographic data offer important information complementary to phase identification in the reconstruction of mineralization sequences. More generally, assessment of the distributions of crystallite size and orientation, in particular preferential orientations (or misorientations) in non-isotropic materials, is crucial for both palaeontological and taphonomic studies as they provide unique information for deciphering the mineralization processes associated with biomineralization, fossilization and/or diagenesis. We should also point out here that variations in the position of a diffraction peak (in 2θ) can be due to a modification of intereticular distances, and thus highlight strain (thermal or mechanical) undergone by the materials during burial or diagenesis. Moreover, resolving crystallographic parameters in the skeleton of problematic extinct microorganisms has been shown (using EBSD in that case) to help in the determination of their affinities [14], and could also be used for larger organisms and/or their tissues.

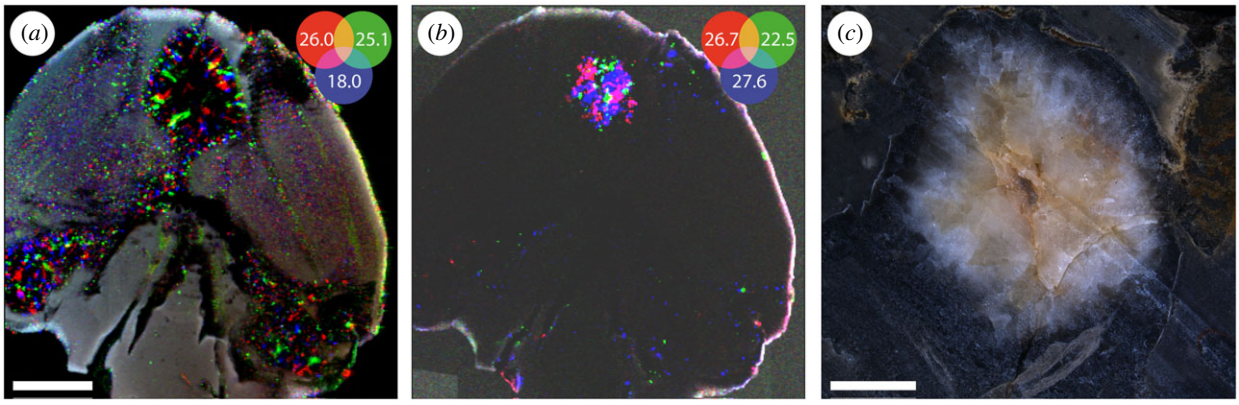

Figure 4. Textured mineralization of the heart in the thylacocephalan arthropod *D. ingens* (specimen MNHN.F.A66910) from the La-Voulte-sur-Rhône Lagerstätte (Jurassic, France). (*a*) False colour overlay of different calcite crystalline planes (for different values of 2θ, in degrees, at 18 keV). (*b*) False colour overlay of different dolomite crystalline planes (for different values of 2θ, in degrees, at 18 keV). (*c*) Optical close-up of the heart, showing some of the elongated crystals of calcite at the periphery and much poorly organized dolomite at the centre. Acquisition parameters: 9×11 µm^2 (H × V) beam spot size, 75×75 µm^2 scan step, 108 900 pixels, 180 ms counting time per pixel (total acquisition time 4 h 51 min). Scale bar = 5 mm in (*a*,*b*) and 1 mm in (*c*).

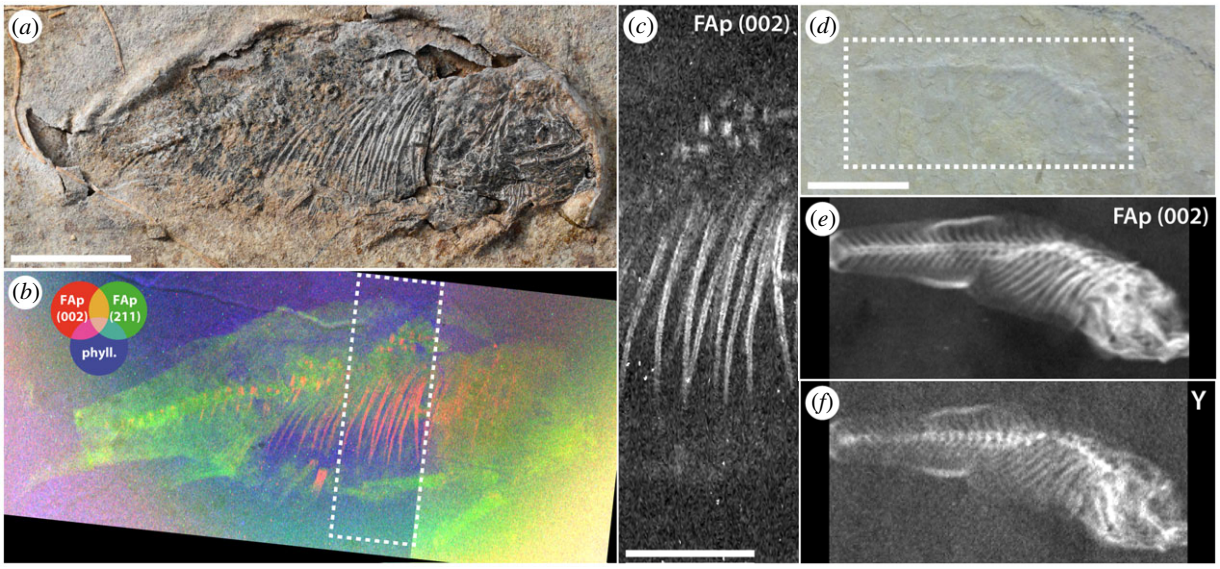

Figure 5. SRS-XRFD imaging of compressed fossil fishes. (*a*) Optical photograph of the osteoglossomorph *L. ancestralis* (specimen 099-PV-DZ-UERJ) from the Sanfransiscana Basin, Quiricó Formation (Barremian, southeastern Brazil). (*b*) False colour overlay of XRD intensity maps for fluorapatite (200) (red) and (211) (green), and phyllosilicates (blue). (*c*) XRD intensity map for fluorapatite (002), close-up from the box area in (*b*). Acquisition parameters: 50×50 µm^2 (H × V) beam spot size, 35×35 µm^2 scan step, 1 182 149 pixels (slightly cropped herein), 30 ms counting time per pixel (total acquisition time 24 h 03 min). (*d*) Optical photograph of a hidden cyprinodontiform *Prolebias goreti* (specimen MNHN.F.CRT255) from the Apt-Céreste-Forcalquier Basin (Rupelian, Céreste-Bastide du bois, southern France). (*e*) XRD intensity map for fluorapatite (002). (*f*) Yttrium distribution from XRF. Acquisition parameters: 100×100 µm^2 (H × V) beam spot size, 100×100 µm^2 scan step, 60 750 pixels (cropped herein), 54 (XRF) and 47.8 (XRD) ms counting times per pixel (total acquisition time 1 h 28 min). Scale bar = 1 cm in (*a*,*b*,*d*–*f*) and 5 mm in (*c*).

3.3. Mineralogical contrasts reveal hidden anatomies

The mineralogical contrasts offered by SRS-XRFD can also be exploited to image compressed fossils that remain difficult (or impossible) to describe using conventional imaging methods such as optical photography and microscopy. We applied SRS-XRFD to two compressed fossil fishes (figure 5), generating up to 1.2-megapixel maps for a specimen of the osteoglossomorph *L. ancestralis* (specimen 099-PV-DZ-UERJ) from the approximately 125-million-year-old Sanfransiscana Basin, Brazil (figure 5*a*,*b*). The distribution of fluorapatite from their skeleton allows for the visualization of their anatomy (figure 5*b*,*e*), with a resolution sufficient to observe tiny details such as central hollow tubes within the ribs of *Laeliichthys* (figure 5*c*). In the case of a specimen of the cyprinodontiform *Prolebias goreti* (specimen MNHN.F.CRT255) from the approximately 30-million-year-old Apt-Céreste-Forcalquier Basin, southern France, hidden within a thin slab of limestone (figure 5*d*), fluorapatite maps even offer a way better contrast (figure 5*e*) than XRF mapping of yttrium (figure 5*f*), an element that preferentially substitutes for calcium in calcium phosphates such as bone apatite, and has been shown to yield useful anatomical contrasts for a wide range of fossils [35]. With an information depth of one to a few millimetres (depending on the energy of the X-ray used and the density of the material), SRS-XRFD mineralogical mapping of fossil slabs that thin, therefore, appears as a promising complement to SRS-XRF elemental mapping, which only gives access, in most fossils, to the first 100 µm at the surface of the sample (see [35]), to reveal hidden anatomies in compressed fossils. Texture can also

provide interesting anatomical contrasts, distinguishing, for instance, between different bones, and scales in *Laeliichthys* (figure 5*b*).

4. Potential limitations

There are three main inherent limitations to SRS-XRFD two-dimensional mapping: (1) the illuminated crystallites need to be in the right geometrical orientation to diffract; (2) the beam spot size should be larger than the size of the crystallites to obtain continuous rings (pending that condition (1) is fulfilled; if the beam size is of similar size or smaller than the crystallites, e.g. for high lateral resolution analyses, only spots will possibly appear on the XRD images); and most importantly (3) as the approach works in transmission geometry, samples have to be thin enough to allow transmission. Conditions (1) and (2) are discussed and illustrated in §3.2 (note that because of condition (1) quantitative phase analyses cannot usually be performed here). Regarding condition (3), maximum sample thickness for a given material depends on the X-ray energy used (the higher the energy, the more X-rays penetrate). Within the 6–30 keV range of energies commonly available at XRD synchrotron beamlines, X-rays can probe up to a few millimetre-thick fossils (depending on the exact photon energy used and the density of the material), such that SRS-XRFD is well-adapted to millimetre-thick cross-sections prepared through three-dimensionally preserved fossils, but also to compressed fossils on slab that thin. It works also with thin sections, though they must be uncovered in order to take advantage of XRF collected synchronously in reflection geometry (the underlying glass slide on which they are mounted is not problematic as it does not produce a sharp diffraction that competes with that of the sample). Nonetheless, finely polished sections (30 µm or below) may not present a sufficient diffracting volume, resulting in a poor signal (or require increased exposure times per point for reasonable statistics); preference should, therefore, be given to sections polished to 100 µm or thicker (not thicker than a few millimetres to allow X-ray transmission; see above).

5. Conclusion

In this paper, we introduce synchrotron rapid scanning transmission XRD, synchronously coupled to X-ray fluorescence mapping (SRS-XRFD), as a novel method of identifying and mapping minerals at the microscale over pluri-centimetric thin fossils and sections, within a reasonable time frame and with bulk sensitivity. XRF major to trace elemental mapping helps phase identification, and informs on trace element incorporations within minerals. Besides phase identification and corresponding lateral distribution in the sample, SRS-XRFD further informs on texture (preferential orientation), crystallite size and local strain, providing unique information to characterize fossil tissues and decipher fossilization processes (figures 1–4). In the examples presented herein, we particularly highlight how pinpointing tissue-specific phase distributions and crystallographic characteristics is instrumental in defining mineralization sequences, reconstructing the fossilization environment, and constraining preservation biases. In addition, this approach offers at least three other promising perspectives for taphonomic and palaeontological research: (i) the ability to similarly characterize both three-dimensional fossils (using cross-sections) and entire compressed fossils, which is hardly possible through the petrographic observation of thin sections, provide a unique way to compare preservation mechanisms at stake in formations that yielded both three dimensions and compressed fossils; (ii) SRS-XRFD could be applied to fossils of the earliest known chordates and vertebrates with the aim to detect the first signs of hydroxyapatite biomineralization (bone) in the fossil record, and to understand how the first forms of bone have evolved, how they were constructed, and their potential functions; and (iii) used in an integrative way, tissue-specific mineralization identified at the locality level could reveal the affinities of enigmatic tissues and/or organisms. Mapping mineral distributions and crystallographic parameters at the microscale could also potentially provide new insight into other (bio)mineralization processes in environmental sciences. Finally, we show that tissue-specific mineralogical compositions, and/or differences with the encasing sedimentary matrix, can represent a new source of contrasts to visualize hidden anatomies in compressed fossils for which X-ray tomography is limited, and/or which are buried too deeply within the sediment for SRS-XRF mapping (figure 5).

Data accessibility. All data used in this work are available from the Dryad Digital Repository: https://dx.doi.org/10.5061/dryad.s7h44j13z [39].

Authors' contributions. C.M., S.R., D.T. and N.L. implemented the setup on the beamline. C.M. developed data processing routines. P.G. and C.M. conceived the study, performed the experiments and processed and interpreted the data. C.C., P.M.B., C.J., S.M. and S.C. provided the samples and helped with data interpretation. P.G., S.R. and C.M. drafted the manuscript. All authors contributed to the final editing.

Competing interests. We declare we have no competing interests.

Funding. This research has been supported by SOLEIL synchrotron. C.C. was funded by the Coordenação de Aperfeiçoamento de Pessoal de Nível Superior—Brasil (CAPES)—Finance Code 001 (Programa Nacional de Pós Doutorado-PNPD) and Programa de Apoio à Docência (PAPD, process no. E-26/007/10661/2019)—UERJ.

Acknowledgements. We are grateful to SOLEIL synchrotron for provision of beamtime, P. Joly for assistance at the DiffAbs beamline, S. Blanchandin and K. Chaouchi for their help with X-ray powder diffraction, as well as J. Berthauld and teams at the control and data acquisition 'software and IT' and 'Electronic systems' groups of SOLEIL synchrotron for the development of the FLYSCAN platform. C. Fossé prepared the rod-shaped sample. A. Pradel and M. Véran provided the accession number for the *Prolebias goreti* specimen. The authors also warmly thank A. Daley for English edits, and the reviewers, whose comments, suggestions and corrections helped to improve the manuscript.

References

1. Briggs DEG. 2003 The role of decay and mineralization in the preservation of soft-bodied fossils. *Annu. Rev. Earth Planet. Sci.* **31**, 275–301. (doi:10.1146/annurev.earth.31.100901.144746)
2. Wilson P, Parry LA, Vinther J, Edgecombe GD. 2016 Unveiling biases in soft-tissue phosphatization: extensive preservation of musculature in the Cretaceous (Cenomanian) polychaete *Rollinschaeta myoplena* (Annelida: Amphinomidae). *Palaeontology* **59**, 463–479. (doi:10.1111/pala.12237)
3. Orr PJ, Briggs DEG, Kearns SL. 1998 Cambrian Burgess Shale animals replicated in clay minerals.

Science **281**, 1173–1175. (doi:10.1126/science.281.5380.1173)

4. Koenig AE, Rogers RR, Trueman CN. 2009 Visualizing fossilization using laser ablation–inductively coupled plasma–mass spectrometry maps of trace elements in Late Cretaceous bones. *Geology* **37**, 511–514. (doi:10.1130/G25551A.1)
5. Bergmann U, Morton RW, Manning PL, Sellers WI, Farrar S, Huntley KG, Wogelius RA, Larson PL. 2010 *Archaeopteryx* feathers and bone chemistry fully revealed via synchrotron imaging. *Proc. Natl Acad. Sci. USA* **107**, 9060–9065. (doi:10.1073/pnas.1001569107)
6. Bergmann U, Manning PL, Wogelius RA. 2012 Chemical mapping of paleontological and archeological artifacts with synchrotron X-rays. *Annu. Rev. Anal. Chem.* **5**, 361–389. (doi:10.1146/annurev-anchem-062011-143019)
7. Wogelius RA *et al.* 2011 Trace metals as biomarkers for eumelanin pigment in the fossil record. *Science* **333**, 1622–1626. (doi:10.1126/science.1205748)
8. Anné J *et al.* 2014 Synchrotron imaging reveals bone healing and remodelling strategies in extinct and extant vertebrates. *J. R. Soc. Interface* **11**, 20140277. (doi:10.1098/rsif.2014.0277)
9. Gueriau P *et al.* 2014 Trace elemental imaging of rare earth elements discriminates tissues at microscale in flat fossils. *PLoS ONE* **9**, e86946. (doi:10.1371/journal.pone.0086946)
10. Gueriau P, Mocuta C, Bertrand L. 2015 Cerium anomaly at microscale in fossils. *Anal. Chem.* **87**, 8827–8836. (doi:10.1021/acs.analchem.5b01820)
11. Gueriau P, Bernard S, Bertrand L. 2016 Synchrotron advanced imaging of paleontological specimens. *Elements* **12**, 45–50. (doi:10.2113/gselements.12.1.45)
12. Schwartz AJ, Kumar M, Adams BL, Field DP (eds). 2009 *Electron backscatter diffraction in materials science*. Dordrecht, The Netherlands: Springer.
13. Cusack M. 2016 Biomineral electron backscatter diffraction for palaeontology. *Palaeontology* **59**, 171–179. (doi:10.1111/pala.12222)
14. Päßler JF, Jarochowska E, Bestmann M, Munnecke A. 2018 Distinguishing biologically controlled calcareous biomineralization in fossil organisms using electron backscatter diffraction (EBSD). *Front. Earth Sci.* **6**, 16. (doi:10.3389/feart.2018.00016)
15. De Nolf W, Dik J, Van der Snickt G, Wallert A, Janssens K. 2011 High energy X-ray powder diffraction for the imaging of (hidden) paintings. *J. Anal. At. Spectrom.* **26**, 910–916. (doi:10.1039/C0JA00255K)
16. Mürer FK, Sanchez S, Álvarez-Murga M, Di Michiel M, Pfeiffer F, Bech M, Breiby DW. 2018 3D maps of mineral composition and hydroxyapatite orientation in fossil bone samples obtained by X-ray diffraction computed tomography. *Sci. Rep.* **8**, 10052. (doi:10.1038/s41598-018-28269-1)
17. Cook PK, Mocuta C, Dufour É, Languille MA, Bertrand L. 2018 Full-section otolith microtexture imaged by local-probe X-ray diffraction. *J. Appl. Crystallogr.* **51**, 1182–1196. (doi:10.1107/S1600576718008610)
18. Leclercq N, Berthault J, Langlois F, Le S, Poirier S, Bisou J, Blache F, Medjoubi K, Mocuta C. 2015 Flyscan: a fast and multi-technique data acquisition platform for the SOLEIL beamlines. In *ICALEPCS 2015, 15th Int. Conf. on Accelerator and Large Experimental Control Systems*, *Melbourne, Australia*, *17–23 October 2015*, abstract no. WEPGF056.
19. Kirkpatrick P, Baez AV. 1948 Formation of optical images by X-rays. *J. Opt. Soc. Am.* **38**, 766–774. (doi:10.1364/JOSA.38.000766)
20. Basolo S *et al.* 2005 XPAD: pixel detector for material sciences. *IEEE Trans. Nucl. Sci.* **52**, 1994–1998. (doi:10.1109/TNS.2005.856818)
21. Pangaud P *et al.* 2008 XPAD3-S: a fast hybrid pixel readout chip for X-ray synchrotron facilities. *Nucl. Instrum. Methods Phys. Res. A* **591**, 159–162. (doi:10.1016/j.nima.2008.03.047)
22. Medjoubi K, Bucaille T, Hustache S, Bérar J-F, Boudet N, Clemens J-C, Delpierre P, Dinkespiler B. 2010 Detective quantum efficiency, modulation transfer function and energy resolution comparison between CdTe and silicon sensors bump-bonded to XPAD3S. *J. Synchrotron Radiat.* **17**, 486–495. (doi:10.1107/S0909049510013257)
23. Le Bourlot C *et al.* 2012 Synchrotron X-ray diffraction experiments with a prototype hybrid pixel detector. *J. Appl. Crystallogr.* **45**, 38–47. (doi:10.1107/S0021889811049107)
24. Mocuta C *et al.* 2013 Fast pole figure acquisition using area detectors at the DiffAbs beamline–Synchrotron SOLEIL. *J. Appl. Crystallogr.* **46**, 1842–1853. (doi:10.1107/S0021889813027453)
25. Charbonnier S. 2009 Un environnement bathyal au Jurassique: le Lagerstätte de La Voulte. *Mémoires du Muséum national d'Histoire naturelle* **199**, 272.
26. Charbonnier S, Audo D, Caze B, Biot V. 2014 The La Voulte-sur-Rhône Lagerstätte (Middle Jurassic, France). *C. R. Palevol* **13**, 369–381. (doi:10.1016/j.crpv.2014.03.001)
27. Wilby PR, Briggs DEG, Riou B. 1996 Mineralization of soft-bodied invertebrates in a Jurassic metalliferous deposit. *Geology* **24**, 847–850. (doi:10.1130/0091-7613(1996)024<0847:MOSBII>2.3.CO;2)
28. Vannier J, Schoenemann B, Gillot T, Charbonnier S, Clarkson E. 2016 Exceptional preservation of eye structure in arthropod visual predators from the Middle Jurassic. *Nat. Commun.* **7**, 10320. (doi:10.1038/ncomms10320)
29. Jauvion C, Bernard S, Gueriau P, Mocuta C, Pont S, Benzerara K, Charbonner S. 2020 Exceptional preservation requires fast biodegradation: thylacocephalan specimens from La Voulte-sur-Rhône (Callovian, Jurassic, France). *Palaeontology* **63**, 395–413. (doi:10.1111/pala.12456)
30. Scherrer P. 1918 Bestimmung der Grösse und der inneren Struktur von Kolloidteilchen mittels Röntgenstrahlen. *Nachrichten von der Gesellschaft der Wissenschaften zu Göttingen, Mathematisch-Physikalische Klasse* **26**, 98–100.
31. Brito PM, Meunier FJ, Clément G, Geffard-Kuriyama D. 2010 The histological structure of the calcified lung of the fossil coelacanth *Axelrodichthys araripensis* (Actinistia: Mawsoniidae). *Palaeontology* **53**, 1281–1290. (doi:10.1111/j.1475-4983.2010.01015.x)
32. Cupello C, Brito PM, Herbin M, Meunier FJ, Janvier P, Dutel H, Clément G. 2015 Allometric growth in the extant coelacanth lung during ontogenetic development. *Nat. Commun.* **6**, 8222. (doi:10.1038/ncomms9222)
33. Cupello C, Meunier FJ, Herbin M, Janvier P, Clément G, Brito PM. 2017 The homology and function of the lung plates in extant and fossil coelacanths. *Sci. Rep.* **7**, 9244. (doi:10.1038/s41598-017-09327-6)
34. Cupello C, Clément G, Brito PM. 2019 Evolution of air breathing and lung distribution among fossil fishes. In *Evolution and development of fishes* (eds Z Johanson, C Underwood, M Richter), pp. 252–262. Cambridge, UK: Cambridge University Press.
35. Gueriau P, Jauvion C, Mocuta C. 2018 Show me your yttrium, and I will tell you who you are: implications for fossil imaging. *Palaeontology* **61**, 981–990. (doi:10.1111/pala.12377)
36. Clément G. 1999 The actinistian (Sarcopterygii) *Piveteauia madagascarensis* Lehman from the Lower Triassic of northeastern Madagascar: a redescription on the basis of new material. *J. Vertebr. Paleontol.* **19**, 234–242. (doi:10.1080/02724634.1999.10011137)
37. Martill DM. 1988 Preservation of fish in the Cretaceous Santana formation of Brazil. *Palaeontology* **31**, 1–18.
38. Martill DM. 1990 Macromolecular resolution of fossilized muscle tissue from an elopomorph fish. *Nature* **346**, 171–172. (doi:10.1038/346171a0)
39. Gueriau P *et al.* 2020 Data from: Visualizing mineralization processes and fossil anatomy using synchronous synchrotron X-ray fluorescence and X-ray diffraction mapping. Dryad Digital Repository. (doi:10.5061/dryad.s7h44j13z)